Design of an Optically Controlled MR-Compatible Active Needle

Seok Chang Ryu,
Stanford University, Stanford, CA 94305 USA

Zhan Fan Quek, IEEE [Student Member],
Stanford University, Stanford, CA 94305 USA

Je-Sung Koh, IEEE [Student Member],
Biorobotics Laboratory, School of Mechanical and Aerospace Engineering, Seoul National University, Seoul 151-742,Korea

Pierre Renaud,
ICube Strasbourg University, CNRS, INSA, 67084 Strasbourg France

Richard J. Black, IEEE [Senior Member],
Intelligent Fiber Optic Systems Corporation, Santa Clara, CA 95054 USA

Behzad Moslehi, IEEE [Senior Member],
Intelligent Fiber Optic Systems Corporation, Santa Clara, CA 95054 USA

Bruce L. Daniel,
Department of Radiology, Stanford University, Stanford, CA 94305 USA

Kyu-Jin Cho, IEEE [Member], and
Biorobotics Laboratory, School of Mechanical and Aerospace Engineering/IAMD, Seoul National University, Seoul 151-742, Korea

Mark R. Cutkosky, IEEE [Fellow]
Stanford University, Stanford, CA 94305 USA

Seok Chang Ryu: seokchang.ryu@childrens.harvard.edu; Zhan Fan Quek: zfquek@stanford.edu; Je-Sung Koh: jskoh@seas.harvard.edu; Pierre Renaud: pierre.renaud@insa-strasbourg.fr; Richard J. Black: rjb@ifos.com; Behzad Moslehi: bm@ifos.com; Bruce L. Daniel: bdaniel@stanford.edu; Kyu-Jin Cho: kjcho@snu.ac.kr; Mark R. Cutkosky: cutkosky@stanford.edu

Abstract

An active needle is proposed for the development of magnetic resonance imaging (MRI)-guided percutaneous procedures. The needle uses a low-transition-temperature shape memory alloy (LT SMA) wire actuator to produce bending in the distal section of the needle. Actuation is achieved with internal optical heating using laser light transported via optical fibers and side coupled to the LT SMA. A prototype, with a size equivalent to a standard 16-gauge biopsy needle, exhibits significant bending, with a tip deflection of more than 14° in air and 5° in hard tissue. A single-ended optical sensor with a gold-coated tip is developed to measure the curvature independently of

S. C. Ryu is now with the Pediatric Cardiac Bioengineering Laboratory, Boston Children's Hospital and Harvard Medical School, Boston, MA 02115 USA

J.-S. Koh is now with Harvard Microrobotics Laboratory, Harvard University, Cambridge, MA 02138 USA

Color versions of one or more of the figures in this paper are available online at http://ieeexplore.ieee.org.

temperature. The experimental results in tissue phantoms show that human tissue causes fast heat dissipation from the wire actuator; however, the active needle can compensate for typical targeting errors during prostate biopsy.

Index Terms

Active needle; mechanism design; medical robots and systems; optical actuation and sensing

I. Introduction

In the field of interventional radiology, diagnostic (e.g., biopsy) and therapeutic (e.g., brachytherapy) procedures are performed using an imaging device for guidance. Magnetic resonance imaging (MRI) is an advantageous method in this context. The radiologist and the patient are not exposed to ionizing radiation, and the images provided by MR scanners have a high level of contrast and sufficient resolution to identify small structures such as early-stage tumors in the human prostate. According to the American Cancer Society, prostate cancer is among the most common cancers in men and the second leading cause of death by cancer for men in the United States.[1] MRI-guided biopsy is, therefore, of particular interest. There are two leading approaches in prostate biopsy: the transrectal approach and the transperineal approach. The former has been widely used with ultrasound imaging devices. Among other drawbacks, however, it raises concerns regarding infection. The latter approach requires a longer needle but can more easily reach certain regions than the transrectal approach [3]. For the transperineal approach, needle deflection is particularly a concern due to its relatively long insertion depth, which is also one of the most significant factors limiting the accuracy of such MRI-guided procedures [4], as summarized in Table I.

In addition, the needles in a transperineal approach should pass the narrow pubic arch before reaching the prostate. Needle or patient manipulation may be necessary [5] to minimize pubic arch interference (PAI). For patients with large prostate volume, approximately 25% have a significant PAI [6]. Angled needle insertion [7], [8] and using a slightly bent needle, about 2 cm from the tip [9], are suggested to avoid the bone in prostate brachytheraphy.

Control of the needle path, initially achieved with a rigid body assumption [10], has thus evolved toward needle steering [11] by including needle–tissue interaction models to predict the behavior of the needle. A simple insertion strategy was introduced in [12]: The bent needle is rotated by 180° when the estimated deflection reaches a given threshold. More complex control strategies have subsequently been developed to compensate for needle deflections and even to avoid anatomical obstacles. In [13] and [14], the authors propose manipulation of the needle from its base, outside the patient body, using a robotic system to create forces and moments on the needle in a similar way to the approach used by clinicians. The stiffness of the tissues at the entry point may limit the effectiveness of such a steering strategy, and the robotic system must be designed to provide mobilities in addition to those required for needle insertion and rotation about the long axis.

---

[1] www.cancer.org/cancer/prostatecancer/detailedguide/prostate-cancer-key-statistics

A nonholonomic kinematic model was proposed in [15] and adopted for the control of asymmetric bevel tip needles. Although this model assumed a rigid tissue environment, experimental results in artificial soft tissue matched the results of simulations [16]. In recent work, a mechanics-based model combining the mechanical properties of both the needle and tissue has been presented [17], [18].

In these previous approaches, operators do not directly steer the needle tip that eventually determines the insertion path. Instead, actuation and control take place at the needle base. In addition, if actuators are used to achieve motions at the base, they take up room, which limits the number of needles that can be used in close proximity.

In [1], we proposed an extension of needle steering using interactions between the needle and tissues. The design consists of a needle capable of active tip bending with an embedded actuator (see Fig. 1) that, in combination with insertion movement and the needle self-rotation, allows it to be steered to reach small tumors or other sites. A similar concept was introduced in [19], with two bendable shape memory alloy (SMA) wire actuated joints. A high bending angle was obtained within gelatin, but the relatively large outer diameter, 3 mm, limits its use in common biopsy procedures. In addition, the SMA wire in bending mode is less efficient compared to tension mode for high force generation.

The present work extends upon previous results to introduce a low-temperature SMA alloy and improved optical heating efficiency for faster response and less tissue heating. Our hypothesis is that direct tip bending will allow compensation for prostate gland motion and deformation, whose averages are 2.6 and 4.8 mm, respectively [20] during insertion. The actuation system is entirely compatible with MRI, and the size is comparable with standard prostate biopsy needles. In comparison with prestrained needles, this bendable distal degree-of-freedom (DOF) can simplify the real-time path planning of the tip, allowing manual needle manipulation without the aid of external robotic needle insertion systems, similarly to [21]. The proposed design is a hybrid solution that can be switched between a common, symmetric tip needle, suitable for use in firm tissue, without activation (due to its sufficient rigidity) and a tip-steerable active needle with optical activation. In addition, the system has embedded sensing, for closed-loop control of the tip orientation. Needle tip actuation can also be combined with base actuation and can provide measurement of tissue properties at the distal end by monitoring the actuation effort required to achieve a given amount of tip bending.

The current studies, however, have a couple of limitations that will be addressed in the future. First is the tissue phantom: There is no appropriate single phantom satisfying both mechanical and thermal properties. For this reason, a thermal phantom was used to investigate the thermal safety with higher laser powers (0.8 and 1.6 W), while a mechanical phantom was used to examine steerability with a reduced power (0.3 W) due to reduced heat dissipation, generating a similar safe temperature profile.

Second is the laser system, which is currently ON/OFF controlled; therefore, only constant optical power is available per trial. Automatic power regulation in the future will improve the needle performance, allowing higher transient power without tissue damage. This paper

focuses on thermal analysis and bending performance in hard tissue under continuous power application.

In Section II, the design of the active needle is introduced focusing on the embedded SMA wire actuator and machined superelastic SMA tube body. The optical actuation and sensing systems are described in Section III. Needle performance is investigated in Section IV, followed by discussion and the conclusion.

II. Design of Active Needle

A. Active Element Design

A biopsy needle is composed of two main parts: an inner stylet and an outer cannula. During a biopsy, the two elements are inserted together to reach the biopsy site. Then, the inner stylet is removed, and a biopsy probe is inserted to perform the biopsy. For the proposed device, the active element is the inner stylet (see Fig. 2). The active element introduces one bendable DOF in the needle body, located near the needle tip for direct control of tip orientation. A 16G polytetrafluoroethylene (PTFE) tube with 150-μm wall thickness (Zeus Inc., Orangeburg, SC, USA) is used as an outer cannula, which also works as a heat insulation layer preventing direct contact of the heated SMA with tissue.

The active bending element is composed of a 20-mm-long, 250-μm-diameter, custom-made SMA wire used as an actuator, a 1.37-mm outer diameter superelastic NiTi tube (Johnson Matthey Medical Inc., West Chester, PA, USA) with laser machined slits (Lumenous Inc., Sunnyvale, CA, USA) making it unidirectionally flexible, and four optical fibers inserted into lumens in a PTFE core (Zeus Inc., Orangeburg, SC, USA) to maintain their alignment. High-density PTFE is relatively transparent to mid-infrared light, allowing most of the emitted power from the optical fibers to reach the SMA wire. Two optical fibers are employed for heating the SMA wire, while two additional fibers constitute the curvature and temperature sensors.

NiTi (also called *nitinol*), the only metal in the needle, is known for its MR-compatibility and biocompatibility. The design takes advantage of two different properties of NiTi: a shape memory effect and a superelastic effect. The shape memory effect describes the ability to recover from a phase transformation at low temperature by heating. This effect is used in actuating the needle. At higher temperatures, i.e., above the transition temperature, NiTi exhibits a superelastic behavior, meaning that it can withstand relatively large strains without yielding. This effect is used for the outer tube of the flexible section of the needle, and employs a NiTi alloy with a lower transition temperature than the actuator.

The shape memory effect of NiTi has been employed for many microscale actuation applications because of its high force density. The advantages of NiTi for thin actively bendable devices have been recognized by other researchers [22], [23] who have used machined NiTi tubes for a continuum robot body and a force sensing microsurgical instrument, respectively. NiTi has, however, several known limitations, including 1) a small working stroke, which may require an amplifying mechanism, 2) the need for electrical insulation when employing Joule or resistance heating, and 3) the need to clamp or restrain

the ends of an actuator without producing local stress concentrations. Due to these issues, SMA has previously been considered less suitable for needles than for larger steerable catheters [24]. The design presented here employs a series of asymmetric machined slits so that contraction of an SMA wire inside the tube will produce unidirectional bending with respect to the slits. Needle rotation allows for bending in the preferred direction with respect to the tissue into which the needle is inserted.

Because of the short distance of the actuating wire from the neutral axis of this thin needle, small contractions of the wire can produce substantial tube bending in the direction of the slits. As seen in Fig. 1, the slits are 30 μm wide and are designed to close as the bending angle increases beyond 10°. With laser heating of the SMA wire, electrical insulation is not needed and electrical currents are avoided, for MR compatibility. A clamping mechanism, consisting of threading the SMA wire through two machined holes at each end (Fig. 2, Cross section A-A), distributes the high recovery stress. Laser welding and additional clamping mechanisms were considered, but laser welding could cause damage and unwanted contraction of the assembled SMA wire, resulting in reduced mechanical strength and working stroke. Instead, a high-temperature epoxy (EP11HTFS Gray, Resin Laboratory Germantown, WI, USA) is applied. In tests, the needle starts bending immediately with the initiation of laser power, indicating that the wire is sufficiently taut.

Commercial 250-μm-diameter SMA wires, e.g., Flexinol (Dynalloy Inc., Tustin, CA, USA), can generate up to 8% strain and up to 10-N force, starting at higher than 70 °C. This temperature, however, is excessively high compared with safe temperatures for human tissues, which are on the order of 45 °C. In this paper, a low-transition-temperature SMA wire (LT wire) is developed (see Section II-C3) and the outer cannula, a sleeve made of PTFE, provides thermal shielding. As seen in Section II-C1, the temperature in a surrounding tissue phantom remains below 45 °C. The diameter of the active section corresponds to an 18G needle. With the external cannula, the overall diameter is 1.67 mm, which is equivalent to 16G devices used for prostate biopsies.

Fig. 3 shows the components of an active needle prototype, a PTFE outer cannula, an inner needle with an active element (comprising slotted NiTi tube and SMA wire as in Fig. 2), and two replaceable 10-mm-long tips. Two different tips, a symmetric tip and a 30° bevel tip, were used to examine the behavior of the active needle in tissue phantoms (see Section IV). These tips contain a small longitudinal groove (not seen in Fig. 3) and can be firmly integrated with the active element using a press-fit into the end of the NiTi tube.

B. Laser Machined NiTi Flexible Tube

The superelastic nitinol tube undergoes a stress-induced martensitic phase transition when the applied stress is higher than its critical stress, allowing it to deform further without a proportional increase in stress. For this reason, and in light of the complex geometry of the slits, a finite-element analysis was conducted to investigate its behavior, using ANSYS with a provided superelastic model based on the Auricchio Algorithm [25], which is also implemented in other packages [26]. This model was validated previously [1] and used to design different NiTi tubes by changing the size of slits. Using the tubes, various needle prototypes were manufactured (see Table II). A long NiTi wire was anchored only at the

distal end and loaded with weights at the proximal end (instead of clamping both ends, as used for actuation) to investigate tube stiffness and bending behavior.

Plastisol gels (M-F Manufacturing Co., Inc., Fort Worth, TX, USA), fabricated by mixing plastic (polyvinyl chloride) with softener, have been used for research in bevel-tip needle steering as tissue phantoms. Their Young's modulus is measured for gels with different mix ratios [18]. In this research, a 4:1 ratio giving a modulus of approximately 40 kPa is used because it corresponds to the hardest human prostate tissue [27]. Additionally, the plastisol gel is sufficiently transparent to measure needle shapes and bending angles using video.

As seen in Fig. 4, the tendon-loaded needles were fixed vertically in air or in the mechanical tissue phantom. With no load, all prototypes followed straight trajectories when inserted into the phantom, neither buckling nor bending during the insertion process. Applying various weights, simulating SMA contraction forces, the tip bending angle was visually measured. Due to the tissue reaction force, flexible tubes like *P3* are preferred, having a larger bending response and sufficient bending stiffness to return to a straight shape when unloaded. In general, the return force corresponds to about 30% of the force generated in activation, according to the ratio of NiTi Young's moduli in martensite and austenite. Because the NiTi tube dominates the overall needle stiffness, the eventual slope of the curves in Fig. 4 corresponds to that of the tubes themselves. However, for small loads of 4 N or less, the slope is reduced due to some unavoidable friction within PTFE lumen and due to the effect of clamping the distal end of the SMA wire which initially produces a reduced moment of arm.

Assuming up to 10 N of SMA force, reasonable for low-temperature activation, *P3* using the most flexible NiTi tube is selected as the preferred design for hard tissues, e.g., prostate. It has sufficient rigidity in the hard tissue phantom, with a tip angle of less than 1° for forces up to 4 N. If necessary, axial rotation of the needle can be used to help recover the initial straight shape after actuation. With *P3*, about 5° is expected in the hardest cancerous prostate tissue (40 kPa), with up to 14° in air. On the other hand, softer tissues, e.g., liver, may require more rigid tubes like *P1* and *P2* to ensure full recovery from bending; however, they also produce less tissue resistance to bending under actuation so comparable tip angles can be expected.

C. Low-Transition-Temperature Shape Memory Alloy Wire

In this section, temperature requirements of LT SMA wire are investigated through thermal experiments using a thermally equivalent tissue phantom and a corresponding finite-element method (FEM) model, followed by the wire fabrication and the test of its force generation capability. Tissue phantom temperatures are also measured to study the potential heat induced tissue damage by an activated needle.

1) Thermal Phantom Experiment—A thermal phantom should have similar thermal properties to human tissue, such as density, specific heat, and thermal conductivity as included in the bioheat equation [28]. For experiments reported here, the terms for blood perfusion and metabolic heat generation are ignored. The internal heat generation is relatively small compared with the thermal energy by the heated needle, while the perfused

blood, which is hard to simulate, delays activation and accelerates cooling, meaning that it further reduces the risk of tissue damage.

In addition to the appropriate thermal properties, the phantom should be stable at high temperature. For these reasons, polyacrylamide gel (PAG) is adopted, which has been used for radio frequency ablation research. According to [31], PAG can resist temperatures up to 100 °C and is optically transparent or translucent even with additional proteins for visualizing the heated area. Davidson and Sherar [29] measured the thermal properties of PAG, compared with human liver tissue properties [30], summarized in Table III. The amounts of materials and fabrication methods for PAG are described in [32].

Optical heating fibers were connected to a 1070-nm Laser (CW Yb fiber laser, VCFL-1000, V-GEN Electro Optics Ltd., Tel-Aviv, Israel) via an optical isolator [see Fig. 5(a)]. This laser was chosen as it allowed precise tuning of the power over a large range. The isolator allows light transmission in one direction, from the laser source to the needle, protecting the laser from reflected light (a necessity given the reflective coating in the needle). A thermocouple (Omega Engineering Inc., Stamford, CT, USA) is inserted through a small slit on the PTFE tube and then attached on the clamped portion of SMA wire outside of the needle using a high-temperature thermal cement. Additional thermocouples are placed on the outer sheath surface and PAG phantom [see Fig. 5(b)]. An optical fiber with a fiber Bragg grating (FBG) is also inserted into the largest lumen, normally used for the curvature sensor, to measure the internal temperature. The FBG is placed at the center of the active element.

At room temperature of 27 °C, 0.8- and 1.6-W power are applied for 10 s, and the temperature changes are plotted in Fig. 6. In addition, the temperature of the clamped SMA wire on the outer surface of the tube, for the case of actuation in air, is added as a red solid line for comparison [see Fig. 6(b)].

For both the needle interior, and for the SMA clamping point on the outside of the needle, the main difference in PAG compared with actuation in air is a dramatically reduced increase in temperature, even when twice the power, 1.6 W, is applied. The role of the tissue phantom as a heat sink also can be observed from the cooling curves, which decrease significantly faster than in air. In addition, there is no significant increase in external temperature for 10 s of actuation due to the heat capacity of the PAG, with less than 5 °C in the PTFE outer sheath and 1.6 °C in PAG at 2-mm distance from the needle. Heat-induced tissue damage is, therefore, not a critical concern with the active needle adopting a short SMA wire. However, heat dissipation in the phantom necessitates a relatively high power and reduces the efficiency and responsiveness of the needle.

2) Thermal Model—The necessary transition temperatures can be determined by investigating the temperature increase required for the internal SMA wire to generate the desired contraction force and strain. Since it is hard to measure this temperature directly, an FEM thermal model of the needle with tissue phantom is built using ANSYS (see Fig. 7) to extrapolate from temperatures at the internal FBG and external thermocouple used in the previous section.

Optical heating is approximated as uniform internal heat generation at the inside SMA wire. As measured in Section III, 80% of the optical power is considered to be absorbed within the needle. Therefore, for the case of 0.8 W of power, 0.64 W of power will be absorbed, modeled as internal heat generation in the 18-mm-long SMA wire section inside the needle. The outer boundary of the tissue phantom and needle outside of the phantom are assumed to be at constant room temperature, supported by preliminary actuation tests.

As plotted in Fig. 7, for the case of 0.8 W of power, simulation results match the experimental results, with some deviation at the beginning of the needle inside temperature plot and in the maximum predicted temperature at the external SMA clamp. Using this FEM model, the estimated SMA actuator temperature (depicted in red) achieves approximately 24 °C temperature increase in 1.5 s with 0.8 W of power. Subsequently, heat loss into the tissue phantom becomes dominant so that the slope is significantly reduced. Finally, the temperature increases to approximately 37 °C in 10 s. The model suggests that an SMA actuator with a lower transition temperature, for example one achieving a maximum force below 70 °C (body temperature plus the temperature increase), will require only 0.8 W of optical power to bend the needle by several degrees in approximately 1 s. For 10 s of activation with a constant power, the outside SMA wire and the outer sheath temperatures in this case increase to just 7 °C and 5 °C above the initial temperature, respectively, so that both are always less than 45 °C.

This 0.8 W power is, therefore, considered a safe upper limit when the needle is activated with a constant power in human tissue. Higher power is only allowed for a short time, for example, when higher tip bending is instantly necessary for a large curvature trajectory correction.

3) Low-Transition-Temperature Shape Memory Alloy Wire Fabrication—The requirements for an LT SMA wire actuator, found from the experiments (see Sections II-B and II-C1) and simulation (see Section II-C2), are summarized in Table IV, to achieve at least 5° tip bending in a hard prostate without thermal tissue damage.

A 250-μm-diameter body temperature SMA wire was selected from Memry Corporation. By annealing it at 475 °C for 1 h, followed by 3 h of slow cooling in the oven, A_s and A_f were set to around 37 °C and 46 °C, respectively, at no-load condition (see Fig. 8), measured with differential scanning calorimetry (DSC, Discovery, Texas Instruments, USA). The needle stiffness, however, increases both A_s and A_f as the needle bends, which can be measured by a loading test. In a universal tensile machine (RB302, R&B Inc., Korea) integrated with a temperature-controlled chamber, SMA temperature and strain changes are monitored, while maintaining an applied external force. At no-load condition, both test results are consistent. The results, therefore, demonstrate that this SMA wire will start contraction immediately on entry into the human body, eliminating any lost motion. When the wire is heated up to 55 °C, the expected force and strain are about 5 N and 3.3%, respectively, reaching 10 N and 3.8% at 67 °C, resulting in about 5° tip bending in the hardest tissue. Considering that the commercial Flexinol wire starts to contract at 70 °C and generates 10 N of force at around 90 °C, the developed LT SMA wire can significantly improve the responsiveness, efficiency, and thermal safety.

III. Optical Heating and Sensing

A. Distributed Side Heating

To promote compactness and effective heat transfer, optical fibers should run parallel to the needle axis and transmit heat over a finite length of the SMA wire (see Fig. 9).

An initial side heating design in [1] was based on the idea of using tilted FBGs. However, a solution with higher heating efficiency and lower cost was obtained by using a glass etching cream (Armour Etch, Armour Products, Hawthorne, NJ, USA). Two fibers are used to heat the SMA wire. Each of these incorporates multiple-side heating elements. For etching, the fibers are held in a PTFE core, with part of the side wall removed to provide access to the fibers.

In initial tests [2], it was observed that an etched region 1.0 mm long emits 35% of the optical power passing along the fiber, and a 1.5-mm-long region emits 50% of the power; regions over 2 mm long emit too much power and make the fibers quite fragile. Therefore, each fiber is prepared with a 1.0-mm region, a 5.0-mm space, a 1.5-mm region, another 4.5-mm space, and a 2.0-mm region, each region emitting approximately one-third of the power in the fiber. The power, finally, transmitted to the fiber tip is measured as less than 1% of the input power. The two prepared fibers are staggered in the needle, to give an approximately uniform heating region 18 mm long [see Fig. 10(a)].

Of the power emitted by the etched regions, only a fraction is directly absorbed by the SMA wire, due to its high reflectivity (approximately 0.5 [33]) and circular profile. The remaining light is reflected and could lead to low efficiency and excessive heating of the outer tube. Because the PTFE core material is highly transparent to IR laser illumination, its power absorption is small. Therefore, it is coated with a sputtered gold layer so that stray illumination is redirected back to the SMA wire and ultimately absorbed (see Fig. 9).

B. Efficiency Evaluation of the Optical Heating System

The reflectivity of NiTi SMA wire is almost constant in the IR region [33]; however, it highly depends on heat treatment condition [34] and surface finish. Therefore, instead of building analytical models, optical power absorption is investigated experimentally (see Fig. 10).

As a metric of power absorption efficiency, the temperature change of SMA wire is measured at three different heating conditions. The core is placed horizontally to maintain a uniform convection coefficient along the wire. Wire temperature is measured using a thermocouple in the middle of the wire. Due to the arrangement, the measured wire temperature is expected to represent the SMA wire temperature. Experiment (a) involves optical actuation using the staggered heating elements inside the multi-lumen PTFE core, but without a gold coating. Experiment (b) uses a PTFE core with a sputtered gold coating. Experiment (c) involves Joule heating actuation with the same coating condition as (b), where various currents are applied to get comparable temperature changes to (b). In this case, an SMA wire of the same diameter is placed in its dedicated channel and connected to short thin lead wires for applying current. The lead wires are bonded to the PTFE core to

avoid wire movement during activation. The resistance for the short wire is calculated as 0.476 Ω in the martensite phase for computing the Joule heating effect.

The electrical resistance of the SMA wire increases when its phase is switching to austenite, complicating the comparison. Therefore, relatively low levels of optical and electrical power were applied in these tests to keep the wire in the martensite phase. The optical power delivered from the laser is set to 206 mW, but is attenuated to 196 mW just before the heating elements by the 4-m lead length between the laser and the needle. The power after the final heating elements is approximately 1 mW. No backreflection at the far end was detected. Therefore, approximately 195 mW of optical power is emitted.

The temperature changes are presented in Fig. 11. In comparison with experiment (a), the temperature in experiment (b) climbs rapidly within 5 s and reaches 23.5 °C above ambient in 15 s. A similar effect is obtained with 171 mW of Joule heating, albeit with a slightly higher maximum temperature, which represents the ideal case.

In summary, the distributed optical heating with a gold coating results in relatively uniform heating of the SMA wire with a heating efficiency approaching 80%, a significant improvement in optical energy absorption compared with previous systems assuming around 50% transfer efficiency [33], [35], [36]. The uniformity of heating also simplifies thermal modeling of the needle in Section II-C2 for comparison with temperatures measured in a tissue phantom.

C. Optical Curvature Sensing

Optical fiber sensing of temperature and curvature is preferred for a slender MR-compatible device. Many approaches exist in the literature including long-period FBGs (see, e.g., [37] for a review) and sensors for which the transmitted light is inversely proportional to the curvature in a treated region (see, e.g., [38] and [39]). The active needle includes one silica optical fiber with standard FBGs for temperature sensing, located near the neutral axis to minimize the effects of bending, and a plastic optical fiber (POF) with a treated section for which light loss is a function of the curvature (see Fig. 12). The measured bending angle can be used to estimate the needle shape, for example, to track the needle tip in the image plane. In addition, once the temperature and curvature are known, the strain on the needle and actuator can be computed using the elastic model for closed-loop control.

The principle of the curvature sensor is that curvature-dependent optical power loss is amplified in a region that has been treated by machining a pattern of grooves on the cladding and into the core. The power loss through this zone decreases or increases due to the closing or opening of grooves by positive or negative bending, respectively, and dominates any light loss along untreated sections of the fiber. In contrast with sensors based on the loss of light between a source at one end and a receiver at the opposite end, the needle sensor requires a single access point for sending and receiving light at the needle base. Hence, the distal end of the fiber is gold coated for reflecting the light (see Fig. 12).

The prototype optical curvature sensor is integrated with a 150-mm-long 18G biopsy needle for the evaluation. A red LED and a phototransistor (IF-E96-R and IF-D93 respectively,

Industrial Fiberoptics, Tempe, AZ, USA) are connected to the machined POF through a 50:50 power ratio, 2-to-1 optical coupler (IF 562, Industrial Fiberoptics, Tempe, AZ, USA). The core material of this POF, polymethyl methacrylate, is known to be highly transparent to red light, but relatively opaque to IR light. For 1 m of fiber length, the light transmission at 1000 nm becomes nearly zero, while red light transmission is 90.[2] Therefore, the IR light emitted by the heating laser does not significantly affect curvature readings at a remote detector.

As presented in [2], a nearly linear relationship is obtained for curvatures up to about 5(1/m), which corresponds to 5° of tip bending. In future versions, the linear range can be increased by machining sharper grooves in the fiber. In this paper, all tip angles and deflections were captured with a camera and then measured using an imaging tool, IMTOOL of MATLAB.

IV. Device Assessment

From Section II-C2, it is expected that with optical activation at a constant 0.8 W of power, the SMA temperature change is about 37 °C at 10 s, while the outer sheath temperature changes up to 5 °Cfrom body temperature, thus always lower than 45 °C.

In this section, the steerability of the needle prototype is investigated, while keeping the SMA wire temperature at or below 70 °C in 10 s, to keep tissue temperatures outside the needle in a safe range. The PAG thermal phantom, however, is inappropriate for examining steering ability of the active needle because of its brittleness, which destroys the thermal contacts between the moving needle and the phantom. Instead, optical actuation tests are performed in the plastisol tissue phantom that matches the mechanical properties of prostate tissue. However, the level of optical power must now be reduced, accounting for the lower thermal dissipation, so as to simulate the SMA temperature profile expected for 0.8 W activation in human tissue.

An FBG sensor was used to monitor the SMA actuator temperature. Although the PTFE layer between the SMA wire and the temperature sensor is thin (50 μm), there may be a small difference between the measured temperature and the maximum SMA wire temperature. Accordingly, a power level is chosen that will keep the measured temperature at the center of the needle at or below 60 °C. With 0.3 W of constant power, the maximum temperature is 58 °C in 12 s (see Fig. 13), satisfying conservative safety requirements.

For this reduced-power activation test in plastisol, a needle prototype is inserted into the tissue phantom by a linear motor with a constant insertion speed of 0.5 mm/s for 12 s; thus, the total insertion depth is 60 mm. Simultaneously, the active needle is given 0.3 W of optical power during the insertion. For comparison, the same test is repeated but with a substituted 30° bevel tip in the same needle and without optical actuation. The final needle shapes of both cases are presented in Fig. 14, demonstrating comparable tip displacements but slightly higher bending curvature with the active needle, due to the active tip bending. For each needle prototype, six insertions were performed, and the results, tip displacement,

[2]http://www.pofeska.com/

and tip angle, defined as the differences between at the distal end and at the entry point, are summarized in Table V. The passive bevel tip needle results in 8.3 ± 0.55mm tip displacement and 5.1 ± 1.48° tip angle, while 7.2 ± 0.96mm tip displacement and 6.5 ± 1.23° tip angle are obtained with the active symmetric tip needle. At around 55 °C, LT SMA wire can generate around 5 N of contraction force, resulting in around 2° tip bending in the static case, which probably causes the additional 1.4° in average in this insertion test, compared with the passive bevel tip needle.

It was also found that the active needle follows a straight trajectory when inserted without actuation [see Fig. 14(c)], matching the behavior of a passive needle with a symmetric tip. As soon as the laser is switched ON, the needle starts to deviate from its straight trajectory. In addition, the active needle enables after-insertion trajectory correction. In this case, the displacement depends on the SMA force and the tip length. With the current prototype and reduced power setting, the after-insertion deflection is small, at 0.87 mm and 5° tip bending. However, the needle can achieve a much larger deflection when activation commences immediately before insertion.

The deflection obtained during insertion, about 7-mm tip displacement for 60-mm insertion, is enough to compensate for either the average needle deflection reported in Table I or the prostate gland motion and deformation [20]. If proper optical power regulation is available, enabling brief high-power activation to achieve a higher tip angle followed by continuous low-power activation to maintain the desired tip angle, this steer-ability of active needle will be further improved. As discussed in the next section, this is a subject for future work.

V. Conclusion and Future Work

In this paper, a new design for an MR-compatible active needle is presented. Combining optical heating and SMA, for its shape memory and superelastic effects, allows us to produce a device matching the size of a standard biopsy needle with active deflection capabilities.

Assuming an available actuation force of 10 N, a laser-machined SMA tube is designed that is stiff enough to be inserted into tissue without bending when unactuated, but will bend 5° in hard prostate tissue and 14° in air when actuated. The tube is assembled with a custom-annealed low transition temperature SMA wire actuator starting its contraction near body temperature and generating approximately 10 N at 67 °C. The use of a low-temperature SMA actuator improves both the responsiveness and the thermal safety of the active needle.

For actuating the needle, an MR-compatible optical heating method using side-etched optical fibers has been presented. The heating system includes multiple etched regions to emit power along a parallel 18-mm length of SMA wire. A gold coating is applied to the surrounding multilumen tube to reflect stray light back to the actuator. The experimental results demonstrate substantially improved efficiency of optical power conversion over simple local heating and heating without a reflective coating.

The needle also includes a single-ended optical curvature sensor based on bending loss. The sensor provides nearly linear performance for small bend angles; greater linearity for larger

angles should be possible by modifying the geometry of the grooves machined into the fiber surface. In combination with internal FBGs for temperature sensing, the bending sensor can be used for the closed-loop control of bending. For a given needle stiffness, the bend sensor can also provide an indication of the properties of the surrounding tissue by monitoring the actuator effort required to maintain a desired bending angle.

The assembled needle was subjected to separate mechanical and thermal tests in plastisol and PAG tissue phantoms, respectively. The thermal tests, in combination with an FEM thermal model, show that for a continuous power of 0.8 W, the temperature of the SMA actuator increases by $37°$, enough to produce the desired 10 N of force, while keeping temperatures in adjacent tissue safely below a maximum of $45°$. With active monitoring of the needle internal temperature and active power control, considerably higher amounts of laser power should be possible for brief periods of time, allowing faster response and larger bend angles in tissue.

Bending tests in a mechanical tissue phantom were conducted at a reduced power level to account for the comparatively poor heat dissipation in plastisol. Nonetheless, deflections of several millimeters were obtained during insertion, comparable with the results obtained from a beveled needle.

The next step in this study is to conduct closed-loop control in *ex-vivo* tissues based on continuous measurement of needle temperature and curvature. As noted above, considerably higher power levels can be tolerated for short periods of time. Subsequently, taking advantage of hysteresis in the SMA actuator and friction in the needle assembly, significantly reduced power levels can be used to maintain a desired curvature. Conversely, needle rotation can be used, when desired, to help the needle recover a straight profile when the laser is turned OFF.

Acknowledgment

References

1. Ryu, SC.; Renaud, P.; Black, RJ.; Daniel, BL.; Cutkosky, MR. Feasibility study of an optically actuated MR-compatible active needle; Proc. IEEE/RSJ Int. Conf. Intell. Robot. Syst; 2011. p. 2564-2569.

2. Ryu, SC.; Quek, ZF.; Renaud, P.; Black, RJ.; Daniel, BL.; Cutkosky, MR. An optical actuation system and curvature sensor for a MR-compatible active needle; Proc. IEEE Int. Conf. Robot. Autom; 2012. p. 1589-1594.

3. Mozer PC, Partin AW, Stoianovici D. Robotic image-guided needle interventions of the prostate. Rev. Urol. 2009; 11(1):7–15. [PubMed: 19390670]

4. Blumenfeld P, Hata N, DiMaio S, Zou K, Haker S, Fichtinger G, Tempany C. Transperinal prostate biopsy under magnetic resonance image guidance: A needle placement accuracy study. J. Magn. Reson. Imag. 2007; 26:688–694.

5. Gibbons EP, Smith RP, Beriwal S, Krishna K, Benoit RM. Overcoming pubic arch interference with free-hand needle placement in men undergoing prostate brachytherapy. Brachytherapy. 2009; 8:74–78. [PubMed: 18793877]

6. Peschel R, King C, Roberts K. Pubic arch interference in permanent prostate implant patients. J. Brachytheraphy Int. 1998; 14:241–248.

7. Ryu B, Bax J, Edirisinge C, Lewis C, Chen J, D'Souza D, Fenster A, Wong E. Prostate brachytherapy with oblique needles to treat large glands and overcome pubic arch interference. Int. J. Radiation Oncol. Biol. Phys. 2012; 83(5):1463–1472.

8. Gellekom MPV, Moerland MA, Battermann J, Lagendijk JJ. MRI-guided prostate brachytherapy with single needle method-a planning study. Radiotheraphy Oncol. 2004; 71:327–332.

9. Wang H, Wallner K, Sutlief S, Blasko J, Russel K, Ellis W. Transperineal brachytherapy in patients with large prostate glands. Int. J. Cancer (Radiat. Oncol. Invest.). 2000; 90:199–205.

10. Buonocore E, Skipper G. Steerable real-time sonographically guided needle biopsy. Am. J. Roentgenol. 1981; 136(2):387–392. [PubMed: 6781264]

11. DiMaio S, Salcudean S. Needle steering and model-based trajectory planning. Proc. Med. Image Comput. Comput.-Assisted Intervention. 2003:33–40.

12. Abolhassani, N.; Patel, R.; Ayazi, F. Effects of different insertion methods on reducing needle deflection; Proc. 29th Annu. Int. Conf. IEEE Eng. Med. Biol. Soc; 2007. p. 491-494.

13. DiMaio SP, Salcudean SE. Needle steering and motion planning in soft tissues. IEEE Trans. Biomed. Eng. 2005 Jun.52(6):965–974. [PubMed: 15977726]

14. Glozman D, Shoham M. Image-guided robotic flexible needle steering. IEEE Trans. Robot. 2007 Jun.23(3):459–467.

15. Webster RJ, Kim JS, Cowan NJ, Chirikjian GS, Okamura AM. Nonholonomic modeling of needle steering. Int. J. Rob. Res. 2006; 25(5/6):509–525.

16. Ding, J.; Stoianovici, D.; Petrisor, D.; Mozer, P.; Avila, R.; Ibanez, L.; Turner, W.; Yankelvitz, D.; Wilson, E.; Banovac, F.; Cleary, K. Medical needle steering for lung biopsy: Experimental results in tissue phantoms using a robotic needle driver; Proc. 8th IEEE Int. Conf. BioInformat. BioEng; 2008. p. 1-5.

17. Misra, S.; Reed, KB.; Benjamin, WS.; Ramesh, KT.; Okamura, AM. Observations and models for needle-tissue interactions; Proc. IEEE Int. Conf. Robot. Autom; 2009. p. 2687-2692.

18. Misra S, Reed KB, Schafer BW, Ramesh KT, Okamura AM. Mechanics of flexible needles robotically steered through soft tissue. Int. J. Robot. Res. 2010; 29(13):1640–1660.

19. Ayvali E, Liang C-P, Ho M, Chen Y, Desai JP. Toward a discretely actuated steerable cannula for diagnostic and theraputic procedures. Int. J. Robot. Res. 2012; 31(5):588–603.

20. Stone NN, Roy J, Hong S, Lo Y, Stock RG. Prostate gland motion and deformation caused by needle placement during brachytherapy. Brachytherapy. 2002; 1:154–160. [PubMed: 15090279]

21. Okazawa S, Ebrahimi R, Chuang J, Salcudean SE, Rohling R. Hand-held steerable needle device. IEEE/ASME Trans. Mechatronics. 2005 Jun.10(3):285–296.

22. Kutzer, MD.; Segreti, SM.; Brown, CY.; Taylor, RH.; Mears, SC.; Armand, M. Design of a new cable-driven manipulator with a large open lumen: Preliminary applications in the minimally-invasive removal of osteolysis; Proc. IEEE/RSJ Int. Conf. Intell. Robots Syst; 2011. p. 2913-2920.

23. He X, Handa J, Gehlbach P, Taylor RH, Iordachita I. A submillimetric 3-DOF force sensing instrument with integrated fiber Bragg grating for retinal microsurgery. IEEE Trans. Biomed. Eng. 2014 Feb.61(2):522–534. [PubMed: 24108455]

24. Glozman D, Shoham M. Flexible needle steering for percutaneous therapies. Comput. Aided Surg. 2006; 11:194–201. [PubMed: 17060077]

25. Ferdinando A. A robust integration-algorithm for a finite-strain shape-memory-alloy superelastic model. Int. J. Plasticity. 2001; 17:971–990.

26. Barrett, PR.; Cunningham, P. Super elastic alloy eyeglass frame design using the ANSYS workbench environment; Proc. Int. ANSYS Conf; 2004.

27. Ahn B, Lorenzo E, Rha K, Kim H, Kim J. Robotic papation-based mechanical property mapping for diagnosis of prostate cancer. J. Endourol. 2011; 25(5):857–857.

28. Pennes HH. Analysis of tissue and arterial blood temperature in the resting human forearm. J. Appl. Physiol. 1948; 1:93–122. [PubMed: 18887578]

29. Davidson SRH, Sherar MD. Measurement of the thermal conductivity of polyacrylamide tissue equivalent material. Int. J. Hyperthermia. 2003; 19(5):551–562. [PubMed: 12944169]

30. Copper TE, Trezek G. Correlation of thermal properties of some human tissue with water content. Aerospace Med. 1971; 42:24–27. [PubMed: 5541087]

31. Zhang B, Hu B, Kuang S, Ying H, Wu R, Li J. A polyacrylamide gel phantom for radiofrequency ablation. Int. J. Hyperthermia. 2008; 24(7):568–576. [PubMed: 18608575]

32. Surowiec A, Shrivastava PN, Astrahan M, Petrovich Z. Utilization of a multilayer polyacrylamide phantom for evaluation of hyperthermia applicators. Int. J. Hyperthermia. 1992; 8(6):795–807. [PubMed: 1479205]

33. Yamaguchi K, One R, Okamura H. Light-driven actuator with energy conversion efficiency in the order of 1%. Appl. Phys. Exp. 2009; 2

34. Bellouard, KFY.; Gessmann, T.; Wang, X.; Vlassak, JJ.; Hafez, M. An investigation of the oxidation of laser and furnace-annealed sputter-deposited Ni-Ti thin films using reflectivity measurements; Proc. Int. Conf. Shape Memory Superelastic Technol; 2004.

35. Nakamura Y, Shimizu K. Optical drive of SMA active forceps for minimally invasive surgery. J. Robot. Soc. Jpn. 1999; 17(3):439–448.

36. Zhao ZM, Chen YM, Yu XL. The parameters selection of SMA optically activated and its application. J. Wuhan Univ. Technol.-Mater. Sci. Ed. 2002; 17

37. James SW, Tatam RP. Optical fibre long-period grating sensors: characteristics and application. Meas. Sci. Technol. 2003; 14(5):R49. [Online]. Available: http://stacks.iop.org/0957-0233/14/i=5/a=201.

38. Gao C, Farrell G. Numerical aperture characteristics of angle-ended plastic optical fiber. Proc. SPIE. 2003; 4876:404–415.

39. Fu Y, Di H, Liu R. Light intensity modulation fiber-optic sensor for curvature measurement. Opt. Laser Technol. 2010 Jun.42(4):594–599.

Biographies

Seok Chang Ryu received the Ph.D. degree in mechanical engineering from Stanford University, Stanford, CA, USA, in 2013.
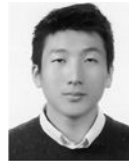
He is currently a Postdoctoral Research Fellow with Boston Children's Hospital and Harvard Medical School, Boston, MA, USA. His research interests include design and control of robotic devices employing smart actuators, sensors and structures, fiber-optic shape and tactile sensors, and advanced manufacturing.

Dr. Ryu was nominated for the Best Medical Robotics Paper Award at the 2014 IEEE International Conference on Robotics and Automation.

Zhan Fan Quek (S'14) received the B.S. degree in mechanical engineering from University of Illinois at Urbana Champaign, Urbana, IL, USA, and the M.S. degree in mechanical engineering from Stanford University, Stanford, CA, USA, where he is currently working toward the Ph.D. degree in mechanical engineering.

His research interests include haptics, teleoperation, and human-safe robotics. His research was supported by a National Science Scholarship, Agency for Science, Technology and Research, Singapore.

Je-Sung Koh (S'10) received the B.S. and Ph.D. degrees in mechanical and aerospace engineering from Seoul National University, Seoul, Korea, in 2008 and 2014, respectively.

He is currently a Postdoctoral Fellow with Harvard Microrobotics Laboratory, Harvard University, Cambridge, MA, USA. His research interests include bioinspired and small-scale robot design with smart materials.

Dr. Koh received the Best Student Paper Award at the IEEE/RSJ EMBS BioRob 2010 and the Compliant Mechanisms Award at the ASME IDETC 2014.

Pierre Renaud received the M.Sc. degree in mechanics and materials from Ecole Normale Suprieure de Cachan, Cachan, France, in 2000 and the Ph.D. degree in robotics from Clermont-Ferrand University, Clermont-Ferrand, France, in 2003.

From 2004 to 2013 he was an Associate Professor with INSA Strasbourg, Strasbourg, France, where he is currently a Professor with the Department of Mechanical Engineering, and a Member of the AVR team at ICube. In 2010 and 2011, he was a Visiting Professor with Stanford University as a Fulbright Fellow. He is a co-founder of Axilum Robotics, a spin-off dedicated to the development of robotized magnetic transcranial procedures.

Richard J. Black (M'84–SM'09) received the B.Sc. (Hons.) degree in physics from University of Canterbury, Canterbury, New Zealand, and the Ph.D. degree in fiber optics from the Research School of Physical Sciences, Australian National University, Canberra, Australia.

He is a Founding Member and Chief Scientist of Intelligent Fiber Optic Systems Corporation, Santa Clara, CA, USA. His research interests include optical fiber sensing systems with application to medical devices, robotics, and structural health monitoring.

Dr. Black is a Life Member of the Optical Society of America, the International Society for Optical Engineers, and the American Institute of Aeronautics and Astronautics.

Behzad Moslehi (M'84–SM'98) received the B.S. degree in electrical engineering from Arya-Mehr University of Technology, Tehran, Iran, in 1978, and the M.S. degree in electrical engineering in 1980, the M.S. degree in applied physics, and the Ph.D. degree in engineering in 1984, all from Stanford University, Stanford, CA, USA.

He is the Founder and Chief Executive Officer/Chief Technology Officer of Intelligent Fiber Optic Systems Corporation, Santa Clara, CA. His research interests include photonic signal processing, sensing, communications, and networking for applications in avionics, safety, life sciences, and energy.

Dr. Moslehi is a Senior Member of the Optical Society of America and the International Society for Optical Engineers, and a Member of the Society for the Advancement of Material and Process Engineering, the Society of Petroleum Engineers, and the American Wind Energy Association.

Bruce L. Daniel received the M.D. degree from Harvard Medical School, Boston, MA, USA, in 1990. He then completed his residency in diagnostic radiology with University of Michigan, East Lansing, MI, USA, in 1995 and a fellowship in cancer imaging with Stanford University, Stanford, CA, USA, in 1997.

He is a Professor of radiology with Stanford University. His research focuses on diagnostic MRI of breast cancer, and MRI-guided interventions, including developing new techniques for MRI-guided prostate biopsy.

Kyu-Jin Cho (M'08) received the B.S. and M.S. degrees from Seoul National University, Seoul, Korea, in 1998 and 2000, respectively, and the Ph.D. degree in mechanical engineering from Massachusetts Institute of Technology, Cambridge, MA, USA, in 2007.

He was a Postdoctoral Fellow with Harvard Microrobotics Laboratory until 2008. He is currently an Associate Professor of mechanical and aerospace engineering and Director of the Biorobotics Laboratory with Seoul National University. His research interests include biologically inspired robotics, soft robotics, and rehabilitation robotics.

Dr. Cho received the 2014 IEEE RAS Early Career Award.

Mark R. Cutkosky (F'12) received the Ph.D. degree in mechanical engineering from Carnegie Mellon University, Pittsburgh, PA, USA, in 1985.

He is Fletcher Jones II Professor in mechanical engineering with Stanford University, Stanford, CA, USA. His research interests include robotic manipulation and tactile sensing and bio-inspired robots.

Dr. Cutkosky's awards include a Fulbright Faculty Chair and NSF Presidential Young Investigator Award. He is a member of Sigma Xi and a Fellow of the American Society of Mechanical Engineers.
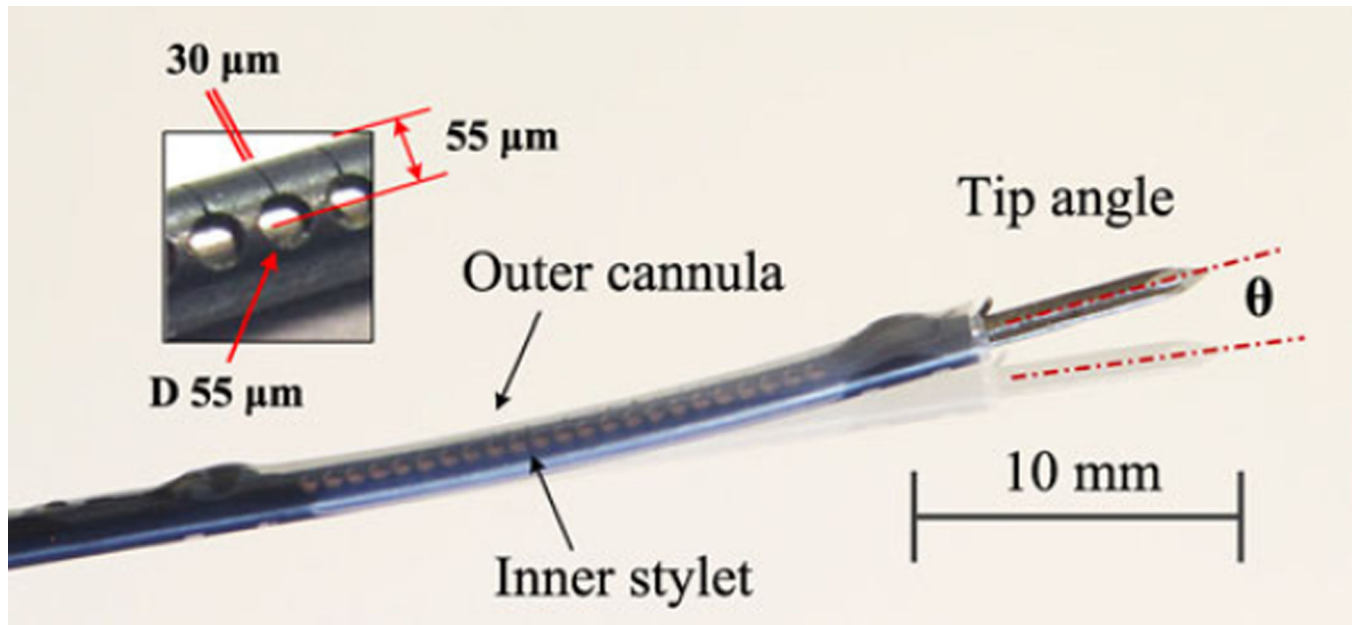
Fig. 1.
Prototype of active needle composed of inner stylet and outer cannula in slightly deflected (8° tip angle) configuration.
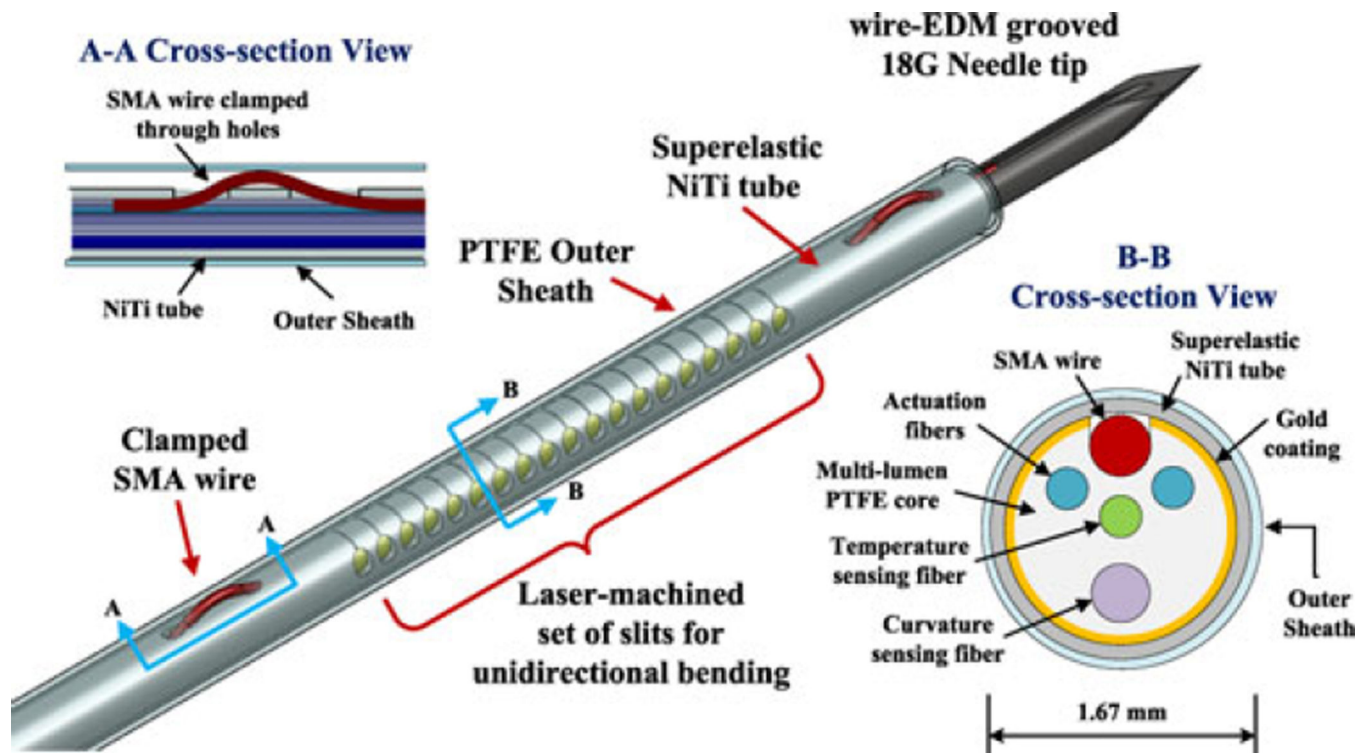
Fig. 2.
Design of the active needle, showing the outer and inner components. Cross-sectional view A-A shows the solution for anchoring the ends of the SMA wire. Cross-sectional view B-B shows inner components, aligned using lumens in the PTFE core. Outermost PTFE tube is used as an outer cannula and a thermal insulation layer.
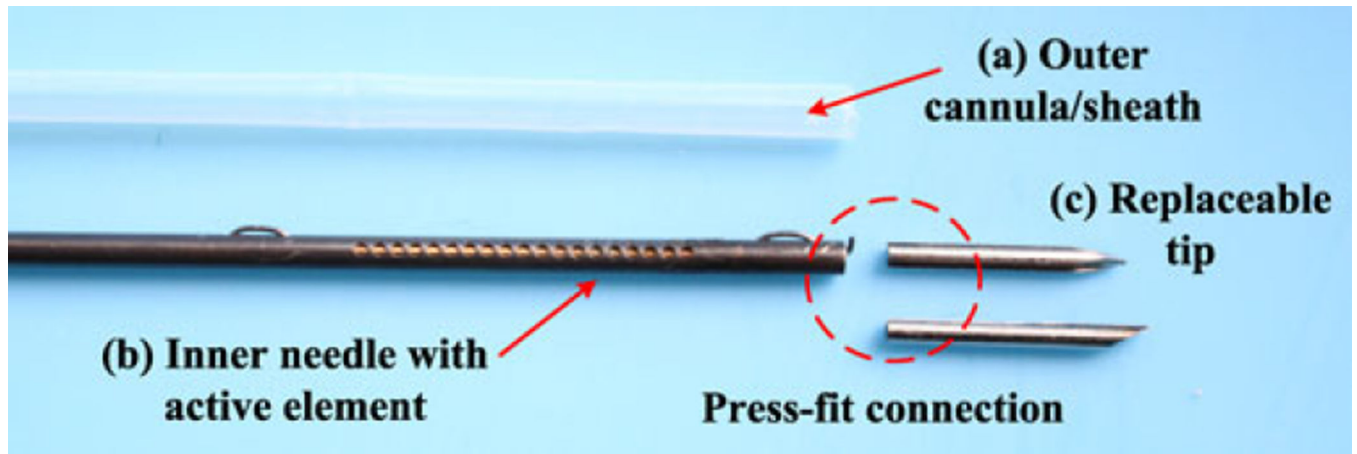
Fig. 3.
Components of active needle prototype: (a) PTFE outer cannula/sheath, (b) inner needle with active element (see Fig. 2 for design details), and (c) replaceable tips (a symmetric tip and a bevel tip).
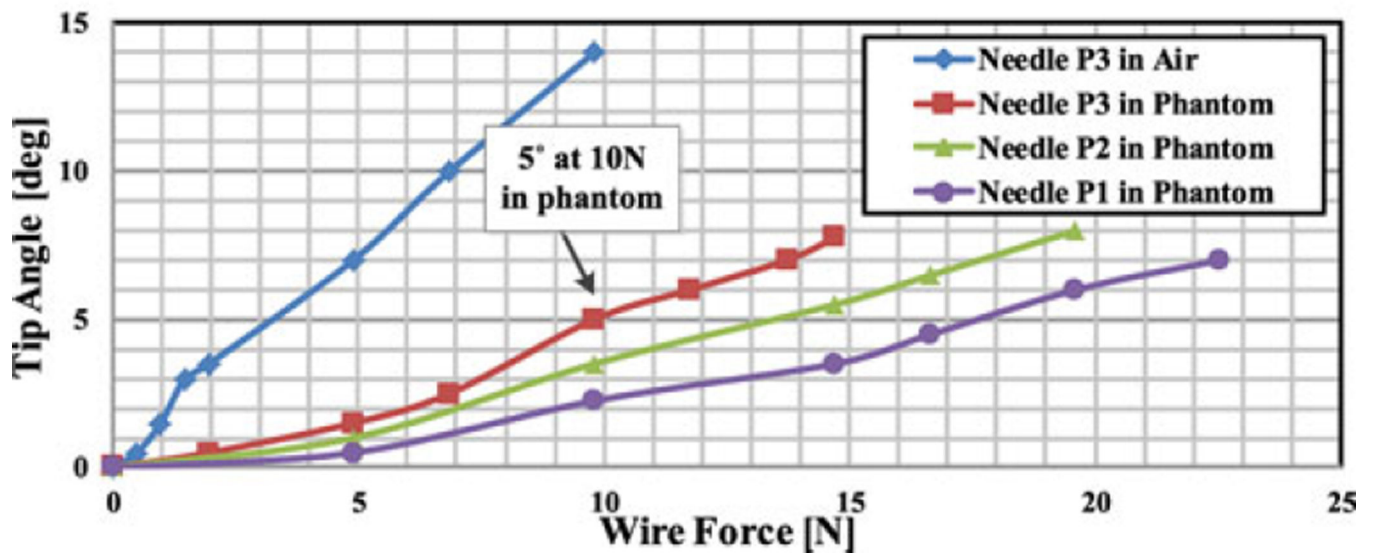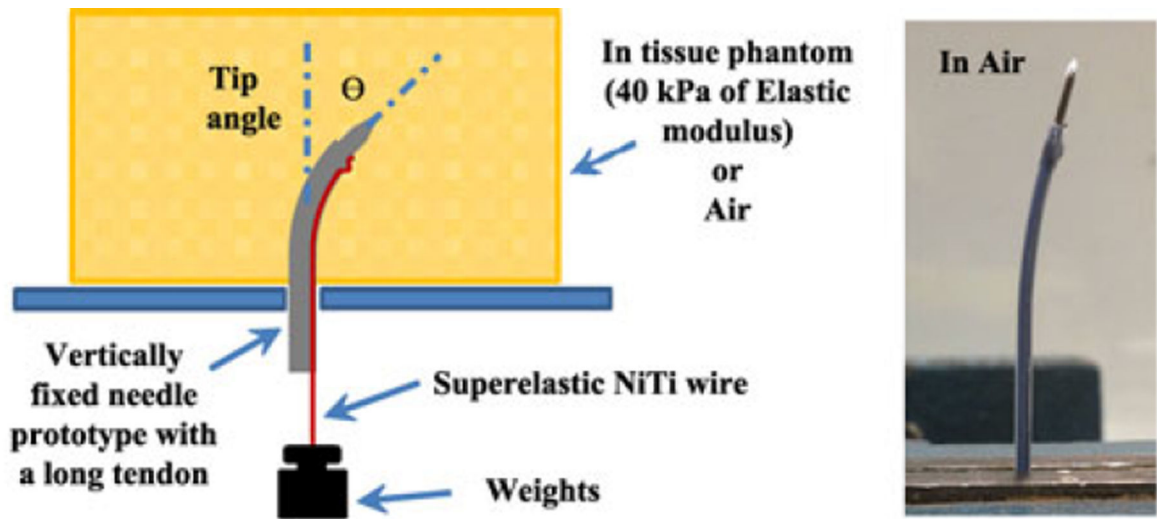
Fig. 4.
Tip angle and SMA wire force relationship with various SMA tubes.
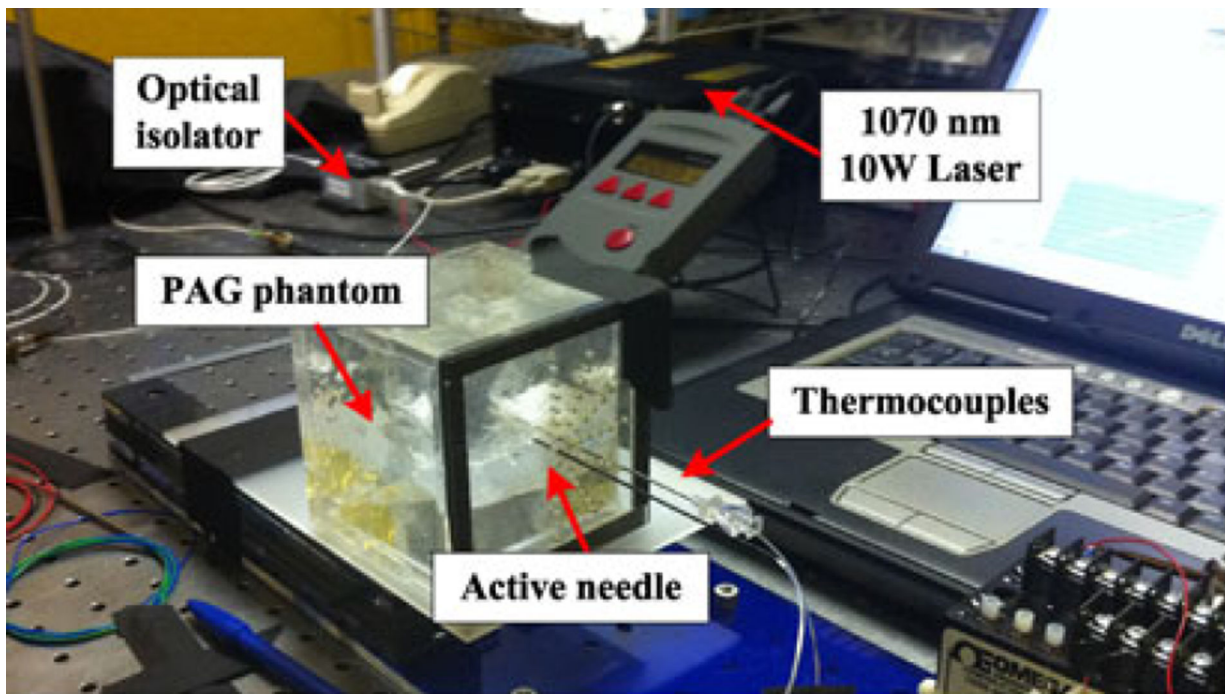
(a)
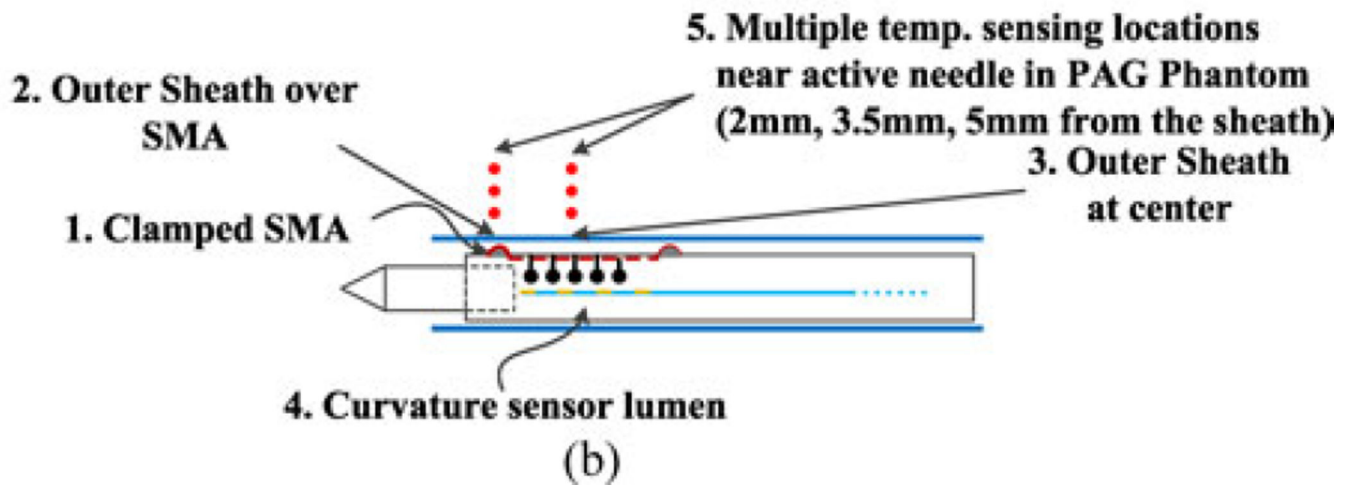
(b)

Fig. 5.
Thermal phantom experiments. (a) Experimental system. (b) Temperature sensing locations
for thermocouples and FBG sensors.
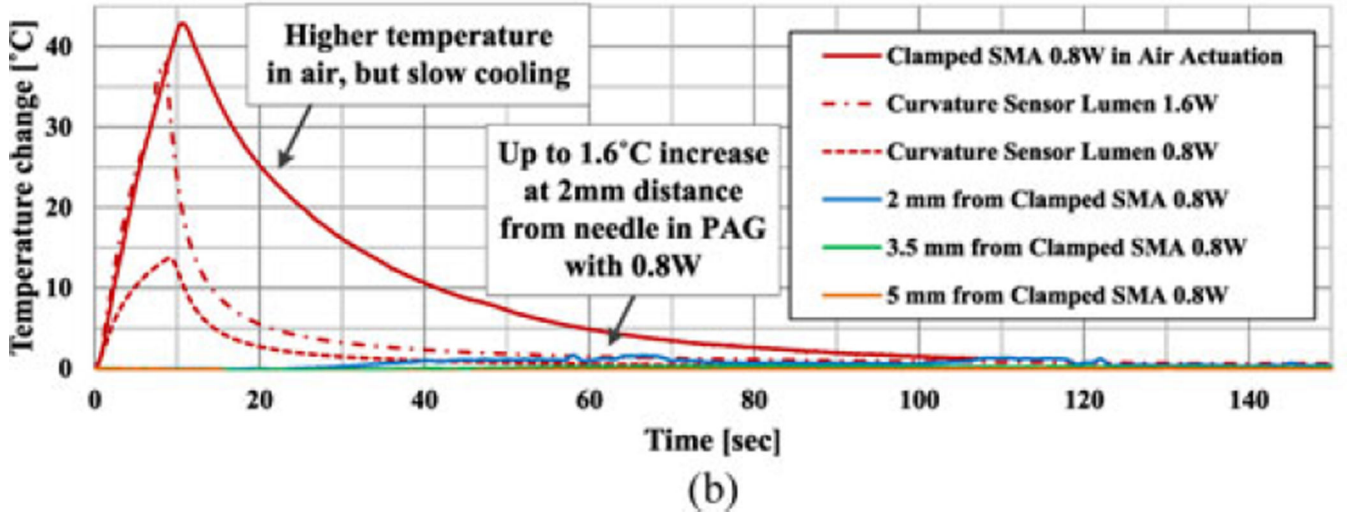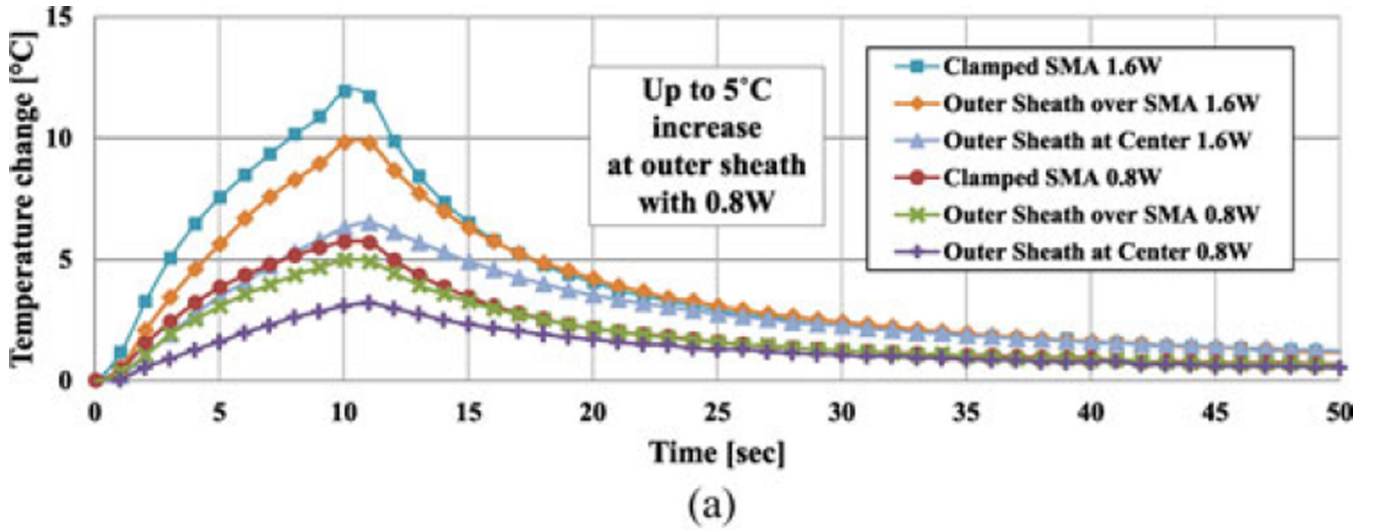
Fig. 6.
Needle and PAG phantom temperature changes. (a) Outer sheath and clamped SMA temperature changes showing up to 5 °C outer sheath temperature change at 0.8-W activation. (b) Curvature sensor lumen and PAG phantom temperature near needle changes showing insignificant tissue temperature changes compared to needle inside.
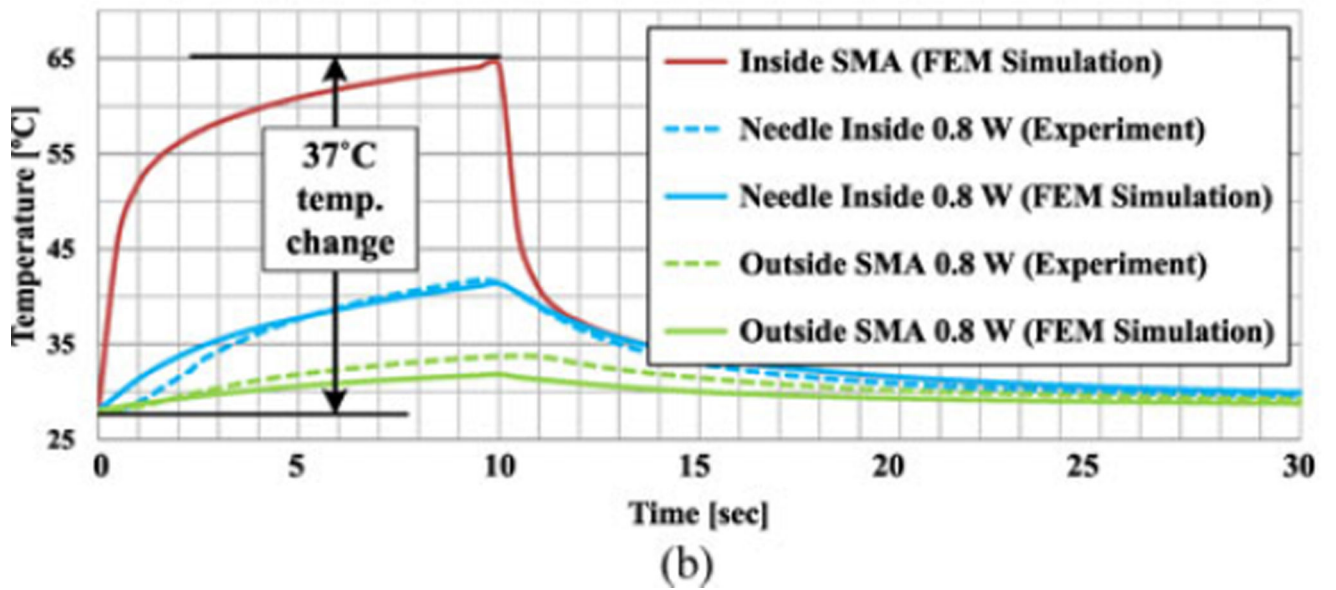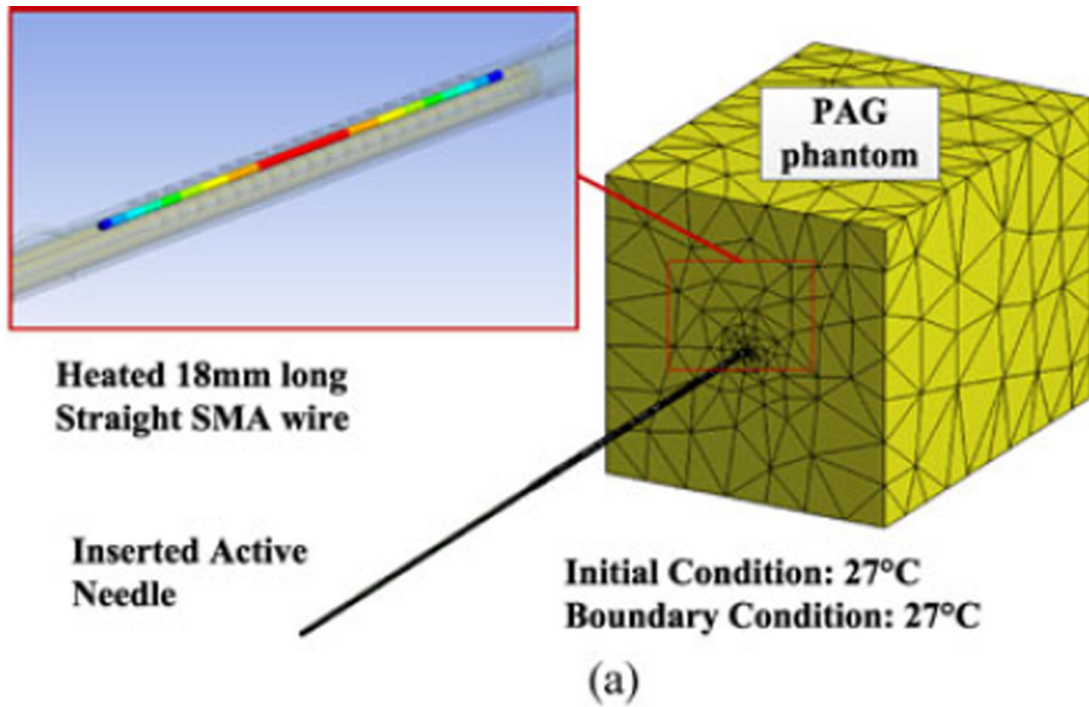
Fig. 7.
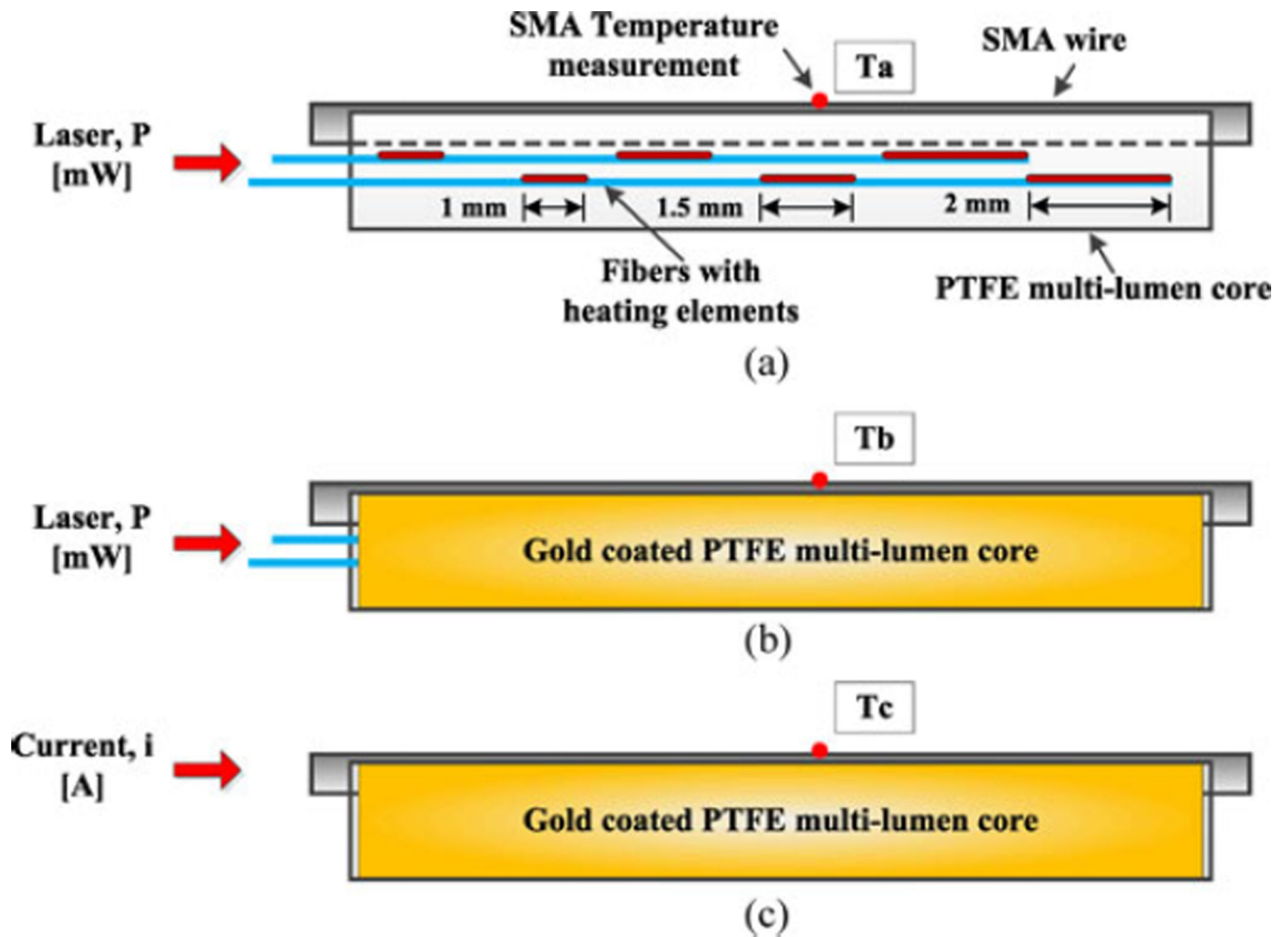Thermal simulation of PAG phantom experiment. (a) FEM model. (b) Estimated SMA temperature in thermal tissue phantom.
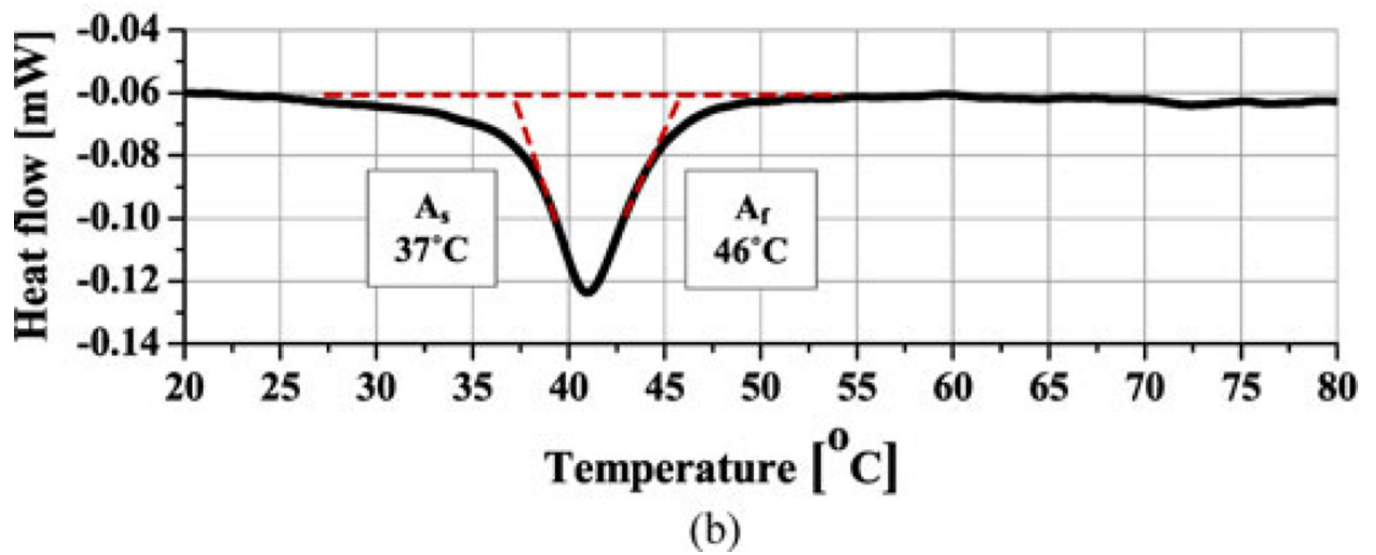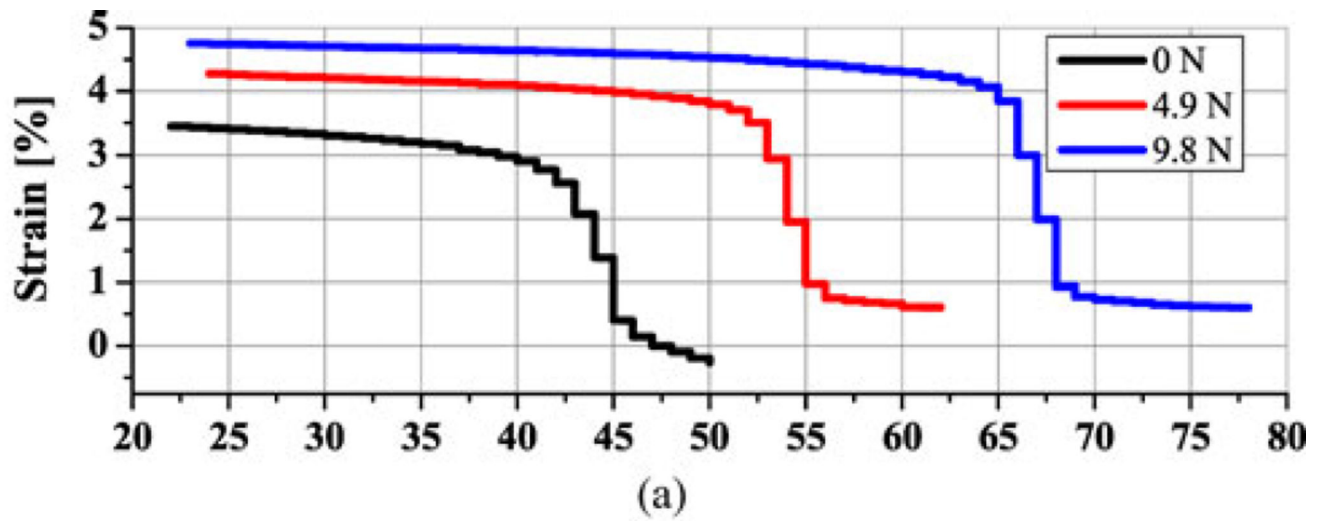
Fig. 8.
Transition temperatures of LT SMA wire actuator. (a) Constant load test showing force and strain generation capabilities. (b) DSC test showing no load transition temperatures.

$$\max P_{abs} = \alpha P_{side} + \alpha(1-\alpha)P_{side} + \cdots$$

Side heating & Gold coat capturing optical power leakage

	SMA wire
	fiber
	gold coat
	light
α	emissivity of SMA
P_{abs}	absorbed power
P_{side}	side power
P_{tip}	tip power
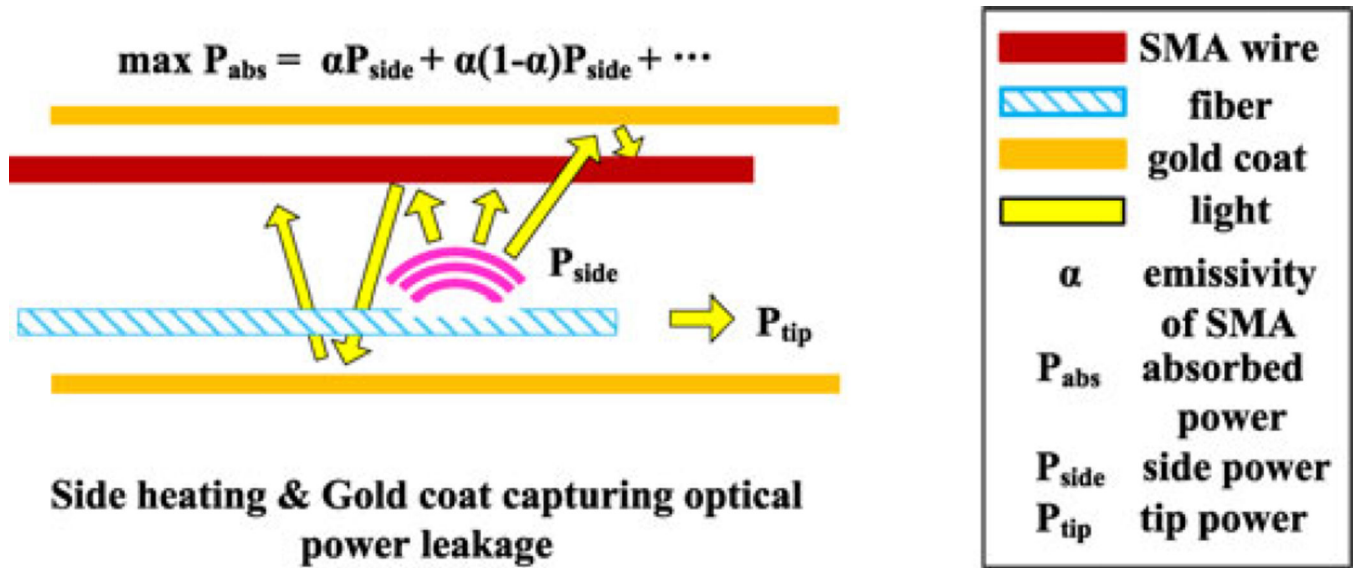
Fig. 9.
Effect of the distributed side heating with gold coat for efficient optical actuation.

Fig. 10.
Experiments for the measurement of optical power transfer efficiency. (a) Optical actuation with the distributed, optimized heating elements (in red) design but without gold coat on the PTFE core; (b) the same condition as (a), but with gold coating; (c) same condition as (b) but with SMA wire heated by electrical current for comparison.
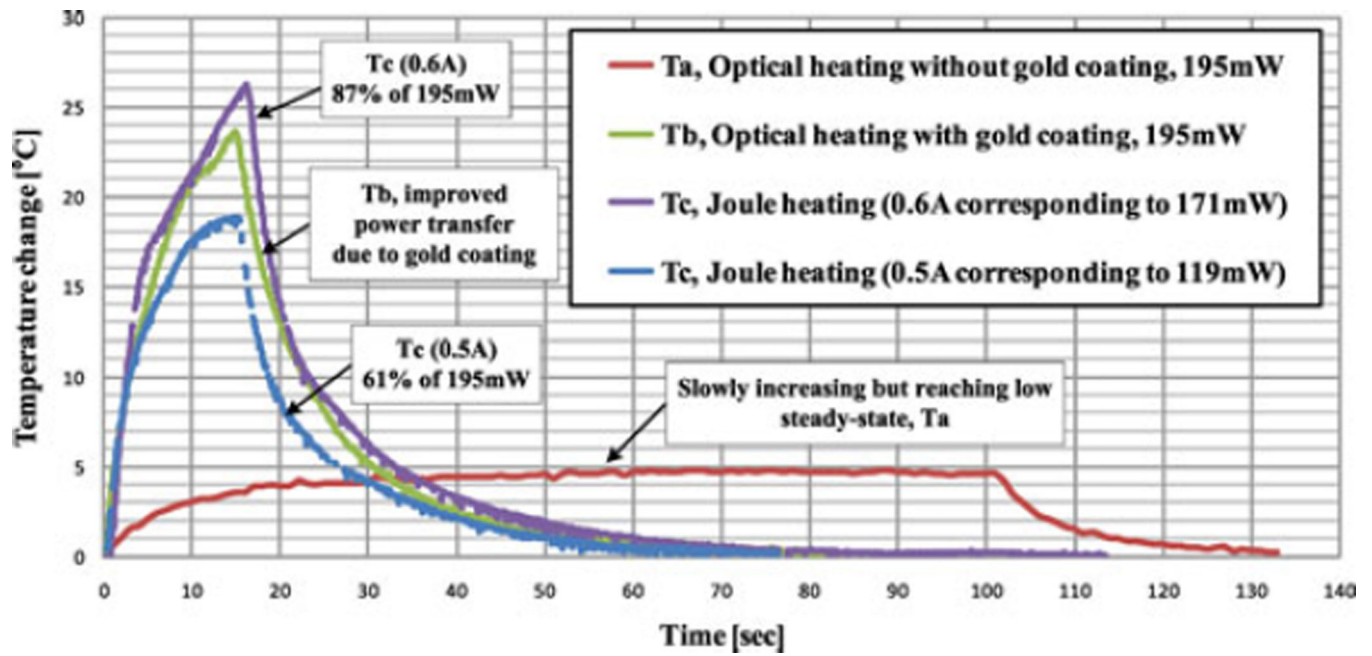
Fig. 11.
SMA temperature change with different heating conditions, measured at the SMA wire center, showing that gold coating significantly improves the optical power transfer efficiency, about 80% compared with Joule heating.
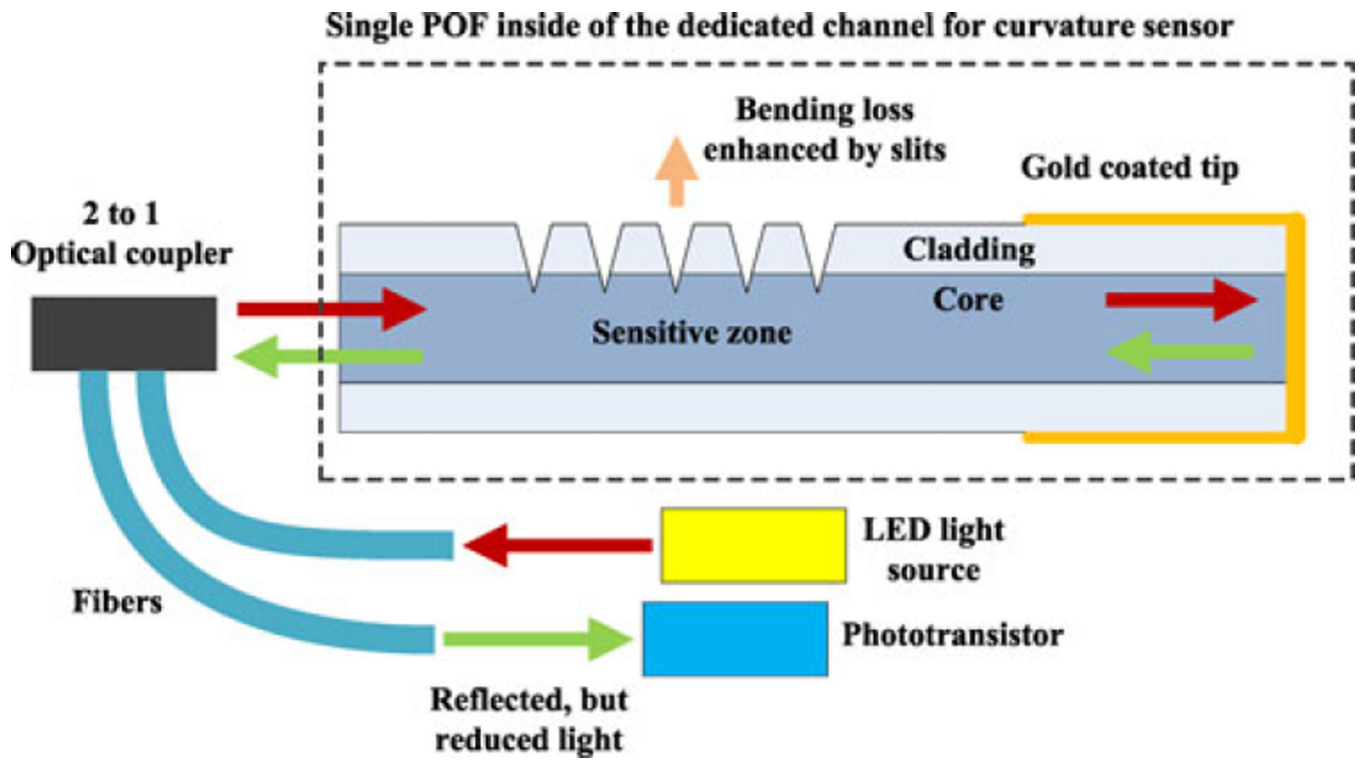
Fig. 12.
Schematic of the single-ended curvature sensor based on enhanced bending loss. A gold-coated tip and 2-to-1 optical coupler enable this sensor to be single-ended.
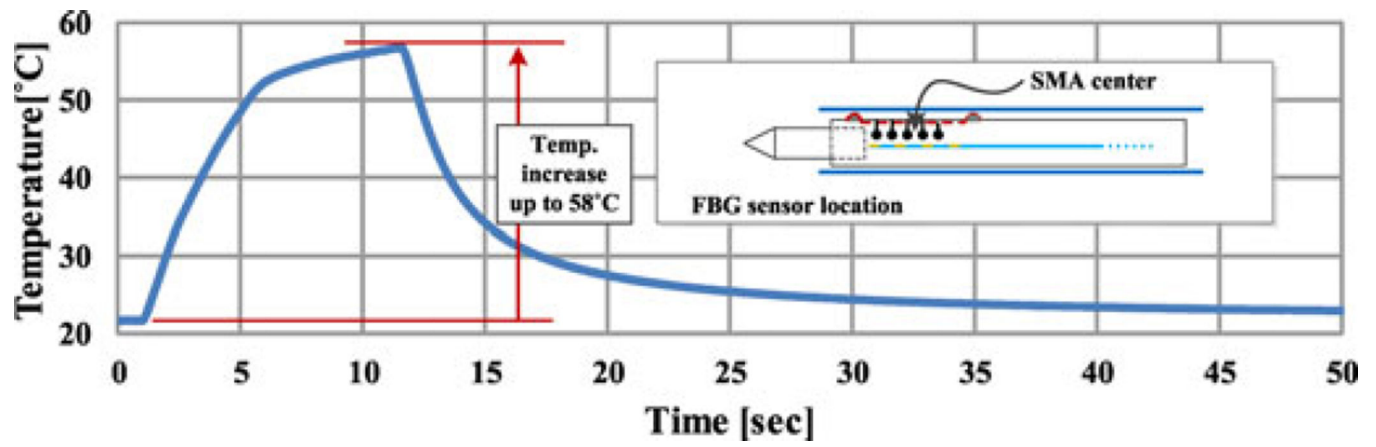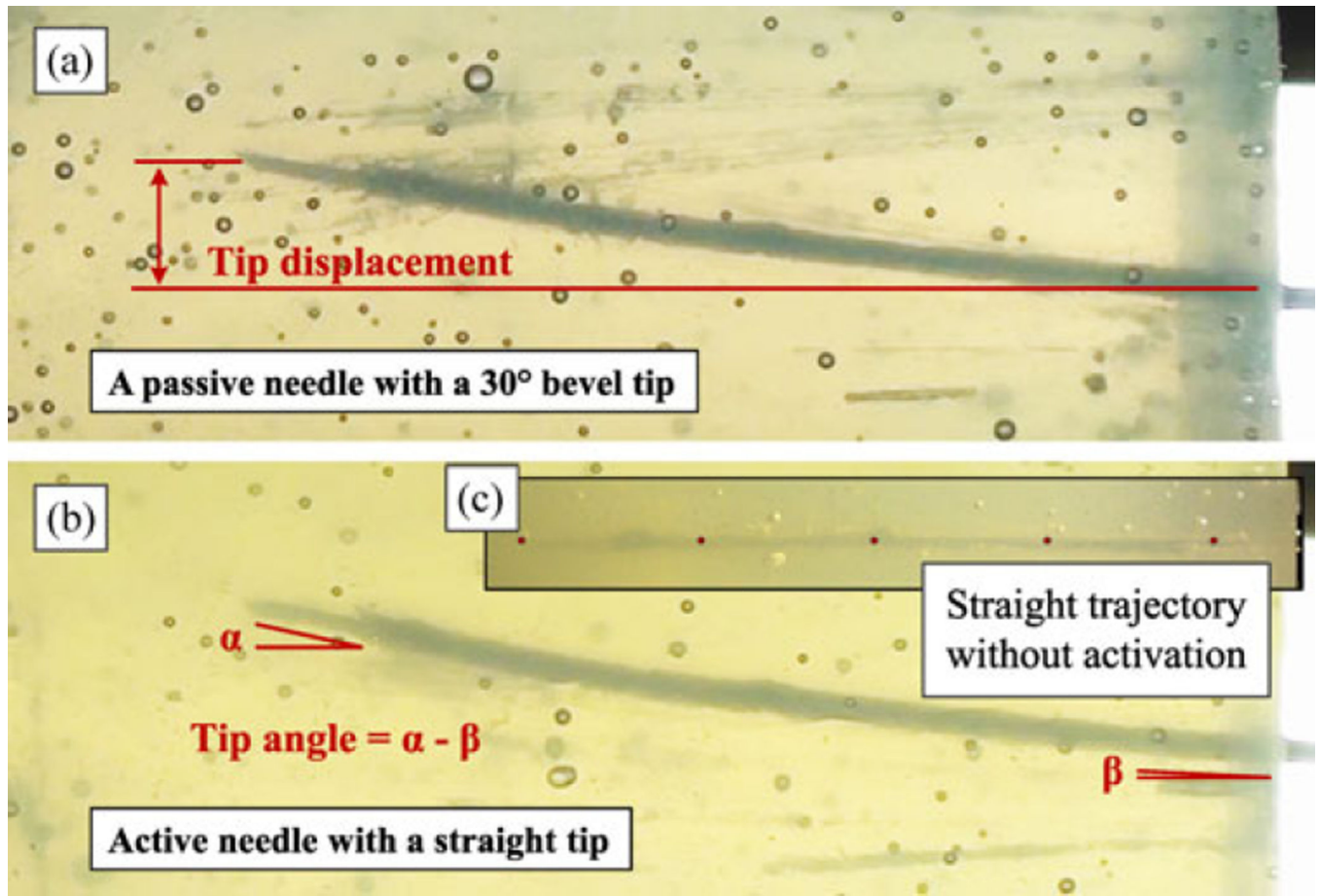
Fig. 13.
SMA temperature change measured with an FBG sensor within the temperature sensor lumen during steerability test.

Fig. 14.
Comparison of a bevel tip passive needle and an active symmetric tip needle insertions. (a) Passive bevel tip needle. (b) Active symmetric tip needle with a comparable deflection. (c)Active symmetric tip needle but without optical actuation, demonstrating a straight insertion trajectory.

TABLE I

Targeting Errors During Needle Insertion [4]

Factor	Target error for 120 mm insertion
Needle deflection	6.5±3.5 mm
Imaging artifact of needle	1.6±0.4 mm
Template misalignment	1.5±0.3 mm

TABLE II

Tendon-Driven Needle Prototypes

Prototypes	Bending stiffness of NiTi tube, equivalent *EI*
P1	1451 N · mm^2 [1]
P2	970 N · mm^2
P3	725 N · mm^2

TABLE III

Thermal Properties of PAG [29] and Human Tissue [30]

Properties	PAG	Human liver
Density [kg/m 3K]	1070	1050
Specific heat [J/kgK]	3810	3612
Conductivity [W/mK]	0.56	0.564

TABLE IV

LT SMA Wire Design Requirements

Properties	Values
Austenite start temperature, A_s	Around body temperature
Austenite finish temperature, A_f	Lower than 70 °C
Force generation	Higher than 10 N at the A_f

TABLE V

Steerability Comparison Test Result

Needle	Tip deviation	Tip angle
Passive 30° bevel tip needle	8.3±0.55 mm	5.1±1.48°
Active needle with a symmetric tip	7.2±0.96 mm	6.5±1.23°